GLIA 55:1334–1347 (2007)

Spatial Arrangement of Microglia in the Mouse Hippocampus: A Stereological Study in Comparison with Astrocytes

SHOZO JINNO,[1]* FRANK FLEISCHER,[2] STEFANIE ECKEL,[2] VOLKER SCHMIDT,[2] AND TOSHIO KOSAKA[1]
[1]*Department of Anatomy and Neurobiology, Graduate School of Medical Sciences, Kyushu University, Higashi-ku, Fukuoka, Japan*
[2]*Institute of Stochastics, Ulm University, Ulm, Germany*

KEY WORDS
Iba1; S100β; point pattern analysis; optical disector

ABSTRACT
Microglia are classically considered to be immune cells in the brain, but have now been proven to be involved in neuronal activity as well. Here we stereologically analyzed the spatial arrangement of microglia in the mouse hippocampus. First, we estimated the numerical densities (NDs) of microglia identified by ionized calcium-binding adaptor molecule 1 (Iba1). Despite that microglia appeared to be evenly distributed throughout the hippocampal area, the NDs demonstrated significant dorsoventral, interregional, and interlaminar differences. Briefly, the NDs in the ventral hippocampus were significantly lower in the CA3 region than in the CA1 region and dentate gyrus, although no interregional differences were detectable in the dorsal hippocampus. Both in the CA1 and CA3 regions, the NDs were significantly higher in the stratum lacunosum-moleculare than in the remaining layers. Next, we investigated the spatial patterns of distribution of Iba1-labeled microglia and S100β-labeled astrocytes. So far as we examined, the somato–somatic contacts were not seen among microglia or among astrocytes, whereas the close apposition between microglia and astrocytes were occasionally detected. The 3D point process analysis showed that the spatial distribution of microglia was significantly repulsive. Because the statistical territory of single microglia was larger than that estimated from process tracing, they are not likely to touch each other with their processes. Astrocytes were distributed slightly repulsively with overlapping areas. The 3D point process analysis also revealed a significant spatial attraction between microglia and astrocytes. The present findings provide a novel anatomical basis for glial research.

INTRODUCTION

Microglia represent a distinct type of resident immune cells in the central nervous system (CNS), which are known to play an essential role in protection of local tissue (for review see, Aloisi, 2001). Over the past few decades, a considerable number of studies have been made to show their morphological and functional changes from the resting to the activated state in response to detrimental stimuli (Hailer et al., 1996; for review see, Schwartz et al., 2006). For instance, Haynes et al. (2006) reported that the microglial branch dynamics is regulated by ATP via purinergic receptor at early stages of response to local CNS injury. Under these circumstances, the resting microglia have increasingly received attention as busy and vigilant housekeepers in recent years. The function of resting microglia has been ensured by recent *in vivo* imaging studies: microglia are highly activated even at the resting state, and continuously survey the local microenvironment (Davalos et al., 2005; Nimmerjahn et al., 2005). The homogeneous distribution of resting microglia seems to be most suitable for enabling them to accomplish the sentinel-like role effectively. In contrast, earlier reports demonstrated that microglia were rather unevenly distributed in various regions of the CNS (Vela et al., 1995). In the hippocampus, Lawson et al. (1990) reported that the dentate gyrus contained more microglia than the Ammon's horn. It has also been reported that microglia are more concentrated in the medial area (presumably corresponding to the stratum lacunosum-moleculare of the Ammon's horn) than in the other areas (Savchenko et al., 2000). However, the numerical densities (NDs; numbers of cells per unit volume) of microglia have rarely been stereologically estimated in the CNS. It is now fairly accepted that the rigorous quantitative data, such as NDs and total numbers, of individual brain components determined by stereological techniques (Sterio, 1984) is a prerequisite for understanding their functional significance. To obtain the accurate NDs of microglia in the hippocampus, here we carried out a stereological analysis using the optical disector (Braendgaard et al., 1990).

Astrocytes, another type of resident glial cells, also play various important roles in the brain, including uptake of neurotransmitters, maintenance of ion homeo-

This article contains supplementary material available via the Internet at http://www.interscience.wiley.com/jpages/0894-1491/suppmat.

Grant sponsor: Japan Society for the Promotion of Science; Grant number: 17300112; Grant sponsors: Sumitomo Foundation (2003), Clinical Research Foundation (2006), DFG Graduate College at Ulm University.

*Correspondence to: Shozo Jinno, Department of Anatomy and Neurobiology, Graduate School of Medical Sciences, Kyushu University, 3-1-1 Maidashi, Higashi-ku, Fukuoka 812-8582, Japan. E-mail: sjnno@med.kyushu-u.ac.jp

Dr. Frank Fleischer's present address is Boehringer Ingelheim Pharma GmbH & Co. KG, Medical Data Services/Biostatistics, 88397 Biberach a.d.R., Germany.

Received 7 February 2007; Revised 19 June 2007; Accepted 21 June 2007

DOI 10.1002/glia.20552

Published online 23 July 2007 in Wiley InterScience (www.interscience.wiley.com).

stasis, and modulation of neuronal functions (for review see, Horner and Palmer, 2003). Especially, they are believed to communicate with microglia via diffusible and nondiffusible factors, such as nitric oxide (Solà et al., 2002), proinflammatory cytokines (Verderio and Matteoli, 2001), and prostaglandins (Mohri et al., 2006). The interaction between microglia and astrocytes comes to the front in some pathological conditions (von Bernhardi and Ramirez, 2001). Although the detailed mechanism underlying their communication has not yet been fully elucidated, the idea of functional interaction allows for the assumption that some kind of spatial relationship between microglia and astrocytes exists. We therefore examined the distribution patterns of microglia and astrocytes and their interrelationship by the point pattern analysis (Diggle, 2003). Here we used the *L*-function, the pair correlation function and the nearest neighbor distance distribution function in combination with the optical disector.

The goal of our study is to provide an anatomical basis for elucidating the role of glial cells in brain function. We identified microglia in the mouse hippocampus by using ionized calcium-binding adapter molecule 1 (Iba1) immunocytochemistry. Iba1 is a 17-kDa EF-hand protein that is specifically expressed in microglia (Imai et al., 1996). As an immunocytochemical marker for astrocytes, we used S100β (Rickmann and Wolff, 1995).

MATERIALS AND METHODS

Every experimental procedure was approved by the Committee of the Ethics on Animal Experiment in Graduate School of Medical Sciences, Kyushu University. All efforts were made to minimize the number of animals used and their suffering.

Tissue Preparations

Eleven adult male C57BL/6J mice (22–25 g body weight, 8–11 weeks old) were used in this study. Animals were deeply anesthetized with sodium pentobarbital (100 mg/kg body weight) and perfused transcardially with phosphate buffered saline (PBS, pH 7.4) followed by a fixative: a mixture of 4% paraformaldehyde, 0.1% glutaraldehyde, and 0.2% picric acid in 0.1 M phosphate buffer (PB, pH 7.4). The brains were left *in situ* for 1–2 h at room temperature and then were removed from the skull. The blocks, including hippocampus and cortex, were dissected out, and divided perpendicularly along the longitudinal hippocampal axis into dorsal, middle, and ventral parts in the same manner as described previously (Jinno et al., 1998). In this study, we analyzed the blocks from dorsal and ventral hippocampi to test the possible dorsoventral differentiation in the spatial arrangement of microglia. Each of hippocampal blocks was cut transversely into 50-μm-thick serial sections on a vibrating microtome (VT1000S; Leica Microsystems, Wetzlar, Germany). To avoid deformation of hippocampus by physical tractions, all sections were processed free-floating with extreme caution.

ABC Immunohistochemistry

After overnight incubation in 1.0% bovine serum albumin (BSA) in PBS containing 0.3% Triton X-100 and 0.05% sodium azide at room temperature, sections were incubated with rabbit polyclonal anti-Iba1 antibody (1:5,000; Wako Pure Chemical Industries, Osaka, Japan) for 5 days at 20°C. Then, they were incubated with biotinylated goat polyclonal anti-rabbit IgG antibody (1:500; Vector Laboratories, Peterborough, UK) for 3 h at room temperature. Next, the sections were processed according to the ABC method (Hsu et al., 1981) with a Vectastain ABC kit (Vector Laboratories). After three washes in PBS and then in 50 mM Tris buffer (TB, pH 7.6), they were reacted with 0.05% diaminobenzidine tetrahydrochloride (DAB; Sigma-Aldrich, St. Louis, MO) solution in 50 mM TB containing 0.01% H_2O_2 for 5–15 min at room temperature. The sections were treated with 0.04% OsO_4 in 0.1 M PB for 30 min to enhance the reaction products, and then dehydrated in graded series of ethanol, infiltrated in propylene oxide, and flat-embedded in Epon-Araldite. Each section was examined under a light microscope (Axioskop 2 MOT; Carl Zeiss, Oberkochen, Germany) equipped with Nomarski optics. Images were photographed with a digital camera (AxioCam; Carl Zeiss) attached to the microscope.

For preparing illustrations, selected digital photomicrographs were processed using an image-editing software package Adobe Photoshop 6.01 (Adobe Systems, San Jose, CA) and a technical drawing software package Canvas 8.06 (ACD Systems, Saanichton, Canada). Only the brightness and contrast were adjusted for the whole frame and no part of a frame was enhanced or modified in any way.

Immunofluorescence Procedure

Sections were incubated overnight with 1.0% BSA in PBS containing 0.3% Triton X-100 and 0.05% sodium azide at room temperature. Then, they were incubated for 5 days at 20°C in mixtures of following primary antibodies raised in different species: rabbit polyclonal anti-Iba1 antibody (1:5,000; Wako Pure Chemical Industries), rat monoclonal anti-Mac-1 antibody (1:500; Serotec, Oxford, UK) and mouse monoclonal anti-S100β antibody (1:10,000; Sigma-Aldrich). After washing three times with PBS, the sections were incubated with a mixture of fluorescein isothiocyanate (FITC)-conjugated donkey anti-rabbit IgG antibody (1:1,000; Jackson ImmunoResearch Laboratories) and Rhodamine Red-conjugated donkey anti-mouse IgG antibody, which also reacted with rat IgG (1:500; Jackson ImmunoResearch Laboratories) for 3 h at room temperature. After three wash with PBS, they were mounted in Vectashield (Vector Laboratories) and examined under a

confocal laser-scanning microscope (CLSM; TCS-SP2; Leica Microsystems).

The penetration of antibodies against Iba1 and S100β into 50-μm-thick section was preliminarily estimated using confocal image stacks. Six sections were selected from three mice, and immunofluorescently stained with Iba1 and S100β. Stacks of 20–30 serial optical sections (voxel size; 0.5 × 0.5 × 2.0 μm) were obtained with a CLSM (TCS-SP2; Leica Microsystems) under a 20× objective lens (NA 0.75), and the cell bodies seen in single optical sections were counted at five different depths of 50-μm-thick sections. The data was statistically analyzed by Friedman's test using a statistical software package Dr. SPSS for Windows (Release 8.0.1J; SPSS Japan, Tokyo, Japan). Because the antibodies against Iba1 and S100β were shown to be adequately penetrated (see results), we used full thickness of 50-μm sections in the following optical disector analysis.

To estimate the size of Iba1-positive ($Iba1^+$) microglia, the stacks of 40–50 optical sections (voxel size; 0.3 × 0.3 × 1.0 μm) were scanned with a CLSM (TCS-SP2; Leica Microsystems) under a 63× oil immersion lens (NA 1.32). The cell bodies and processes of randomly sampled $Iba1^+$ microglia were carefully traced through serial optical sections (see results), and the contours of projection area were measured by using an image-analysis software package ImageJ 1.35 (NIMH, Bethesda, MD). The data were corrected with an average areal shrinkage factor of Vectashield mounted preparations (0.93; Jinno et al., 1998). Equivalent circle radius (ECR) was calculated for soma and processes by assuming their circular shape.

Numerical Densities of $Iba1^+$ Microglia

Prior to the optical disector analysis, we checked the shrinkage and deformation of hippocampus caused by the experimental procedure, because they are critical factors in meaningful estimation of the numerical densities. As a pilot experiment, five sections were randomly selected from the dorsal and ventral hippocampi, respectively, and then processed for Iba1 immunohistochemistry in accordance with the ABC method. The photomicrographs of hippocampus were captured before and after the processing with a light microscope (Axioskop 2 MOT; Carl Zeiss) equipped with a digital camera (AxioCam; Carl Zeiss). In all cases, the size of hippocampus was reduced with no appreciable uneven deformation (Fig. S1). Next, we estimated the areal shrink ratio in individual hippocampal layers, because each of the layers exhibited different content of cell bodies, dendrites, and myelinated fibers (Fig. S2). The data were compared among layers, dorsal, and ventral levels, and their interaction by two-way analysis of variance (ANOVA) for repeated measures (Excel 2003; Microsoft, Redmond, WA). The differences in the areal shrink ratio were not significant among layers [$F(10,88) = 0.36$; $P = 0.55$] nor between dorsoventral levels [$F(1,88) = 0.79$; $P = 0.64$] nor in the interaction of layers versus dorsoventral levels [$F(10,88) = 0.30$; $P = 0.98$]. The absence of laminar differences indicates a uniform shrinkage of hippocampus in our analysis.

Four mice were selected to estimate the numerical density (NDs) of $Iba1^+$ microglia in the mouse hippocampus. Three randomly sampled sections were taken from the dorsal and ventral hippocampal blocks, respectively. As a result, a total of six sections were used for each animal. The sections were processed according to ABC immunocytochemistry, and were examined with a light microscope (Axioskop 2 plus; Carl Zeiss) connected to an image analysis workstation (IntelliStation Z Pro; IBM Japan, Tokyo, Japan). Low power images (650 × 486 μm^2) were randomly photographed from each region of the hippocampus, using a digital camera (CoolSNAP; Roper Industries, Duluth, GA) under a 10× objective lens (NA 0.30). An unbiased counting frame (629 × 461 μm^2) was superimposed on the captured image, which was printed on a laser printer (LBP-870; Canon, Tokyo, Japan) for a mapping work. The upper limit of the optical disector (look-up plane) was set at the top of the section, and the lower limit was set at the bottom of the section. The criteria for counting a microglial cell were that a top edge of Iba1-stained soma was at its best focus within the height of the optical disector and within the counting frame. Cells touching the look-up plane of the optical disector or the exclusion line of the counting frame were not counted. The counting procedure was performed under a 40× objective lens (NA 0.75), which gave a final magnification of 400× with a 10× ocular lens. To avoid double sampling, disector-counted $Iba1^+$ cells were mapped on the printed photomicrographs.

Numerical data was separately obtained from each layer, and then pooled for the CA1, CA3 regions, and the dentate gyrus. The border between the CA1 and CA3 regions was defined with a straight line that linked the termination of the stratum lucidum and the tip of the suprapyramidal blade of the dentate gyrus. We did not separate the CA2 region from the CA1 and CA3 regions, because it was difficult to clearly define the CA2 region based on the Iba1 immunocytochemistry. The area of each hippocampal layer was measured with an image-analysis software package ImageJ 1.35 (NIMH). The ND of $Iba1^+$ microglia in each hippocampal layer was then calculated by using the formula

$$\mathrm{ND} = \Sigma Q - /(A \times H/\mathrm{SV})$$

where ΣQ- was the number of disector-counted $Iba1^+$ cell bodies, A was the area of the hippocampal layer, and H was the height of the optical disector. SV was the volumetric shrinkage factor. Because our pilot study showed the lack of laminar difference in the shrink ratio of Epon-Araldite embedded preparations, here we applied the estimated mean value of SV (0.65) to individual layers. The data were reported as the mean ± standard deviation (SD) among four animals. The dorsoventral differences were tested with Welch's t-test using Excel 2003 (Microsoft), and the significant difference was considered to occur when a P value of <0.05 for the

two-sided test was obtained. The interlaminar and interregional differences were tested by one-way ANOVA with Scheffe's test using a statistical software package Dr. SPSS for Windows (Release 8.0.1J; SPSS Japan).

Spatial Point Pattern Analysis

Nine sections from five mice were randomly selected for the 3D point pattern analysis. They were immunofluorescently processed for Iba1 and S100β. Acquisition of 3D images was carried out by a CLSM (TCS-SP2; Leica Microsystems). Stacks of 20–30 serial optical sections (voxel size; 0.5 × 0.5 × 1.7 μm) were obtained from dorsal CA1 region under a 20× objective lens (NA 0.75). Here we used the optical section at the top (or bottom) cut surface as look-up section, and those remainings as reference sections. The $Iba1^+$ or $S100\beta^+$ cell bodies contained only in the reference optical sections were marked, and their *x*-*y*-*z* coordinates were determined by using an image-analysis software package ImageJ 1.35 (NIMH). The top of soma was used to define the 3D coordinate.

In advance of the calculation, the coordinates of microglia and astrocytes were three-dimensionally corrected with an average shrinkage factor of sections mounted with Vectashield (Jinno et al., 1998): the contraction in *x*- and *y*-axis corrected with a square root of areal shrinkage factor (0.93), and that in *z*-axis was corrected with an average of thickness shrinkage factor (0.70).

For the analysis of point patterns, so called bivariate point process characteristics are used, which not only allow qualitative knowledge about the point patterns but quantify them for specific regions of point pair distances. As a reference model the stationary Poisson point process is used where the points are scattered independently. Besides this scenario of complete spatial randomness (CSR) for the stationary Poisson point process, different behaviors of attraction and repulsion between the points of a certain point pair distance exist. In case of attraction we observe more point pairs of this distance than in case of CSR. In case of repulsion, there are fewer point pairs of this distance than in case of CSR, i.e., the points reject each other and there exists a hard core distance between all points of the point pattern. The point process characteristics which are considered here are the *L*-function $L(r)$, the pair correlation function $g(r)$, and the nearest neighbor distance distribution function $D(r)$, where their definitions and interpretations are similar for the bivariate as for the univariate point pattern. The *L*-function $L(r)$ refers to the scaled mean number of other points in a ball (with radius r) around a randomly chosen point of the point pattern. The pair correlation function $g(r)$ is related to the relative frequency of point pairs with distance r. The difference between these two characteristics is that in case of the *L*-function we consider point pairs with a distance less or equal than r and in case of the pair correlation function we consider point pairs with exactly distance r. The nearest neighbor distance distribution function is the distribution function of a randomly chosen point to its nearest neighbor. Hence $D(r)$ is the probability that a randomly chosen point has a distance less or equal to r than its nearest neighbor. Since these three characteristics deal with point pairs, the generalizations in case of a bivariate point pattern with two marks, e.g., astrocytes and microglia, is the following: we consider point pairs in which one point is of the first type and the other point is of the second type.

Analytical formulae of these characteristics are known for the Poisson point process, and thus comparing the estimated functions of the point pattern with the theoretical ones leads to conclusions for the spatial distribution and the interaction of the points (see "Appendix A" for the formal definitions and estimators of these characteristics). The *L*-function, the pair correlation function and the nearest neighbor distance distribution function were calculated for the point patterns consisting of locations of microglia and astrocytes. Furthermore, the Monte Carlo rank test was performed to test on complete spatial randomness (CSR), and *r*-wise confidence intervals were calculated for the Poisson point process (see "Appendices B and C"). To investigate the spatial behavior of microglia to astrocytes and *vice versa*, bivariate point process characteristics were estimated. In this case, the Monte Carlo rank test and the computation of confidence intervals were based on bootstrap methods (Effron and Tibshirani, 1994; Mattfeldt and Fleischer, 2005).

Data analysis was performed using the GeoStoch library, which has been developed by the Institute of Applied Information Processing and the Institute of Stochastics of Ulm University (see Mayer et al., 2004, http://www.geostoch.de).

RESULTS

Identification of Microglia and Astrocytes

Both Iba1 (Imai et al., 1996) and Mac-1 (CD11b; Perry et al., 1985) are known to be specific immunocytochemical markers for microglia. Previous studies reported the distributions and total numbers of resting microglia in the dentate gyrus of the mouse hippocampus by using Mac-1 immunocytochemistry (Long et al., 1998, Wirenfeldt et al., 2003), but the distribution of Iba1 in the mouse hippocampus has not yet been fully delineated. To start this study, we tested whether the patterns of expression of Iba1 corresponded to those of Mac-1 by double immunofluorescence (Fig. 1A–C). In all hippocampal areas, Iba1 and Mac-1 were almost always detected in the same profiles, which typically exhibited small somata with thin tortuous and ramified processes. These morphological characteristics indicated that Iba1 and Mac-1 could label microglia equally well in the mouse hippocampus. It should be also noted that the labeling patterns of Iba1 and Mac-1 differed at the subcellular level: Iba1 was found both in the cytoplasm and presumably nucleus (inset of Fig. 1A), whereas Mac-1 was detected only at the scant cytoplasm (inset of Fig.

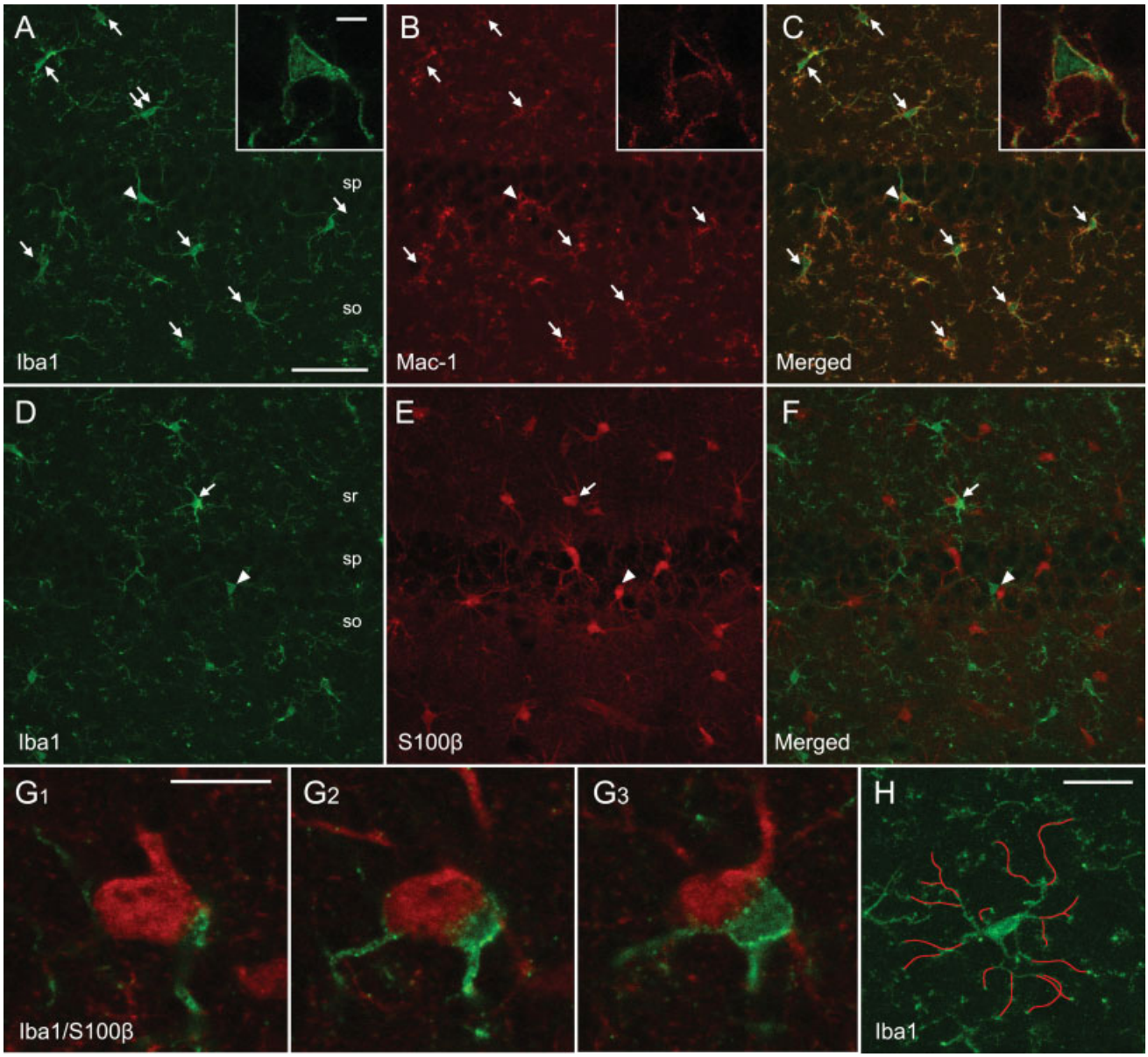

Fig. 1. Immunocytochemical visualization of microglia and astrocytes in the CA1 region by confocal microscopy. **A–C**: Projection images of double immunofluorescence for Iba1 (A), Mac-1 (B), and merged (C). All Iba1$^+$ cell bodies (arrows in A) are immunoreactive for Mac-1 (arrows in B). The insets are high-power micrographs showing an example of the double-labeled cell body of microglia (arrowheads in A–C). It should be noted that Iba1 is observed both in the nucleus and cytoplasm, whereas Mac-1 is detected merely in the thin cytoplasm. **D–F**: Projection images of double immunofluorescence for Iba1 (D), S100β (E), and merged (F). Some of the Iba1$^+$ microglia and S100β$^+$ astrocytes are in contact with each other. Arrows demonstrate an example of the somato–somatic contact between Iba1$^+$ microglia and S100β$^+$ astrocyte. Its detail is shown in **G**. Arrowheads indicate another example of direct contact. $G_{1–3}$: High-power serial optical sections showing direct contact between Iba1$^+$ microglia and S100β$^+$ astrocytes. **H**: High-power projection image of a single Iba1$^+$ microglia (double arrows in Fig. 1A). Red lines represent the processes traced through the serial stacked images. Scale bars: A = 50 μm (applies to A–F); inset of A = 5 μm (applies to inset of A–C); G_1 = 10 μm (applies to G_1–G_3); H = 20 μm. so, stratum oriens; sp, stratum pyramidale; sr, stratum radiatum.

1B). Consequently, it was quite difficult to discriminate rim-like soma from sturdy processes based on the Mac-1 immunocytochemistry. Because our aim was to count the cell bodies of microglia according to the optical disector principle, we decided to use Iba1 as a microglial maker in the present analysis. In contrast, here we used S100β as an astrocyte marker. Although some oligodendrocytes are also labeled by S100β (Ludwin et al., 1976), our previous study (Ogata and Kosaka, 2002) reported that only 1.6% of S100β-positive cells expressed an established oligodendrocyte marker 2P,3P-cyclic nucleotide 3P-phosphodiesterase (CNPase). Thus, we considered that the possible inclusion of oligodendrocytes to S100β$^+$ glial cells would be negligible to the present stereological analysis on the astrocytes.

We next checked the spatial relationship between microglia and astrocyte by using double immunofluorescence for Iba1 and S100β (Figs. 1D–F). The majority of

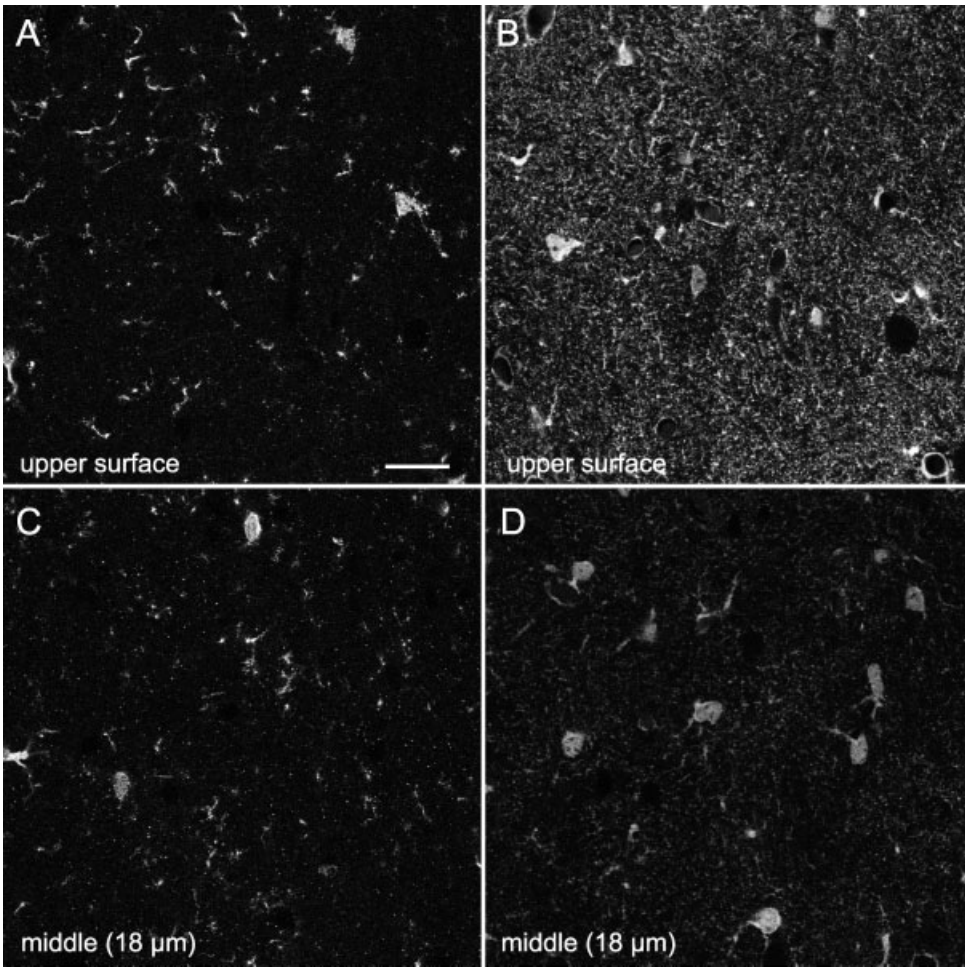

Fig. 2. Confocal optical section stacks showing the penetration of Iba1 (A,C) and S100β (B,D) immunostaining in the mouse hippocampus. **A**,**B**: Confocal micrographs of double immunofluorescence for Iba1 (A) and S100β (B) at the upper surface of the section. **C**,**D**: At 18 μm from the upper surface, the labeling of fine processes identified by S100β is weakened, but the numbers of cell bodies labeled by Iba1 and S100β showed no appreciable reduction. Because section thickness is reduced to 35 μm after mounting with Vectashield, 18 μm from the upper surface represent the middle level. Scale bar: D = 50 μm (applies to A–D). so, stratum oriens; sp, stratum pyramidale; sr, stratum radiatum.

Iba1$^+$ microglia and S100β$^+$ astrocytes showed no apparent relationship in the hippocampal area. But we occasionally encountered the somato–somatic apposition between two different types of glial cells (arrows and arrowheads in Figs. 1D–F). So far as we examined, the mutual contacts were seen neither among microglia nor among astrocytes. In some cases, the somata and processes of S100β$^+$ astrocytes were partially surrounded by the processes of Iba1$^+$ microglia. The high resolution images obtained from the confocal microscopy indicated the direct contact between microglia and astrocytes (Figs. 1G$_{1–3}$). To further examine their interrelationship, we performed a 3D point pattern analysis (see later).

Penetration of Immunostaining

As described previously (Jinno and Kosaka, 2002), the penetration of immunostaining is a critical issue for the optical disector analysis employing thick preparations. The height of counting space should always be adjusted appropriately to the thickness of the sections showing adequate immunostaining. In this study, we planned to apply the optical disector principle to quantitative and point pattern analyses using Iba1 and S100β immunocytochemistry. We therefore preliminarily tested the penetration of antibodies against Iba1 and S100β in 50-μm-thick sections using confocal image stacks. Although the fine S100β$^+$ labeling was reduced at the middle of section (Fig. S3), the numbers of cell bodies identified by Iba1 or S100β staining showed no noticeable differences between cut surface and middle level (Fig. 2). To further examine the z-axis distribution of labeled cells, we counted the numbers of somata seen in the single optical sections at five different depths of 50-μm-thick sections (Fig. S4). Depth-effect was calculated utilizing Friedman's test, and we found no significant difference in the cell numbers along z-axis (χ^2 = 2.887; P = 0.577). These results indicate the adequate penetration of Iba1 and S100β immunostaining for cell counting.

General Description of Iba1$^+$ Microglia

To estimate the size of microglia, the somata and processes were traced through the serial confocal optical sections (Fig. 1H). In the healthy mouse brains we analyzed, Iba1$^+$ microglia typically displayed a small soma (Projection area = 49.5 μm^2; ECR = 3.9 μm; n = 52) with expanded ramified processes (Projection area = 3,263.7 μm^2; ECR = 32.2 μm; n = 41). Morphological changes of microglia from the resting to the activated

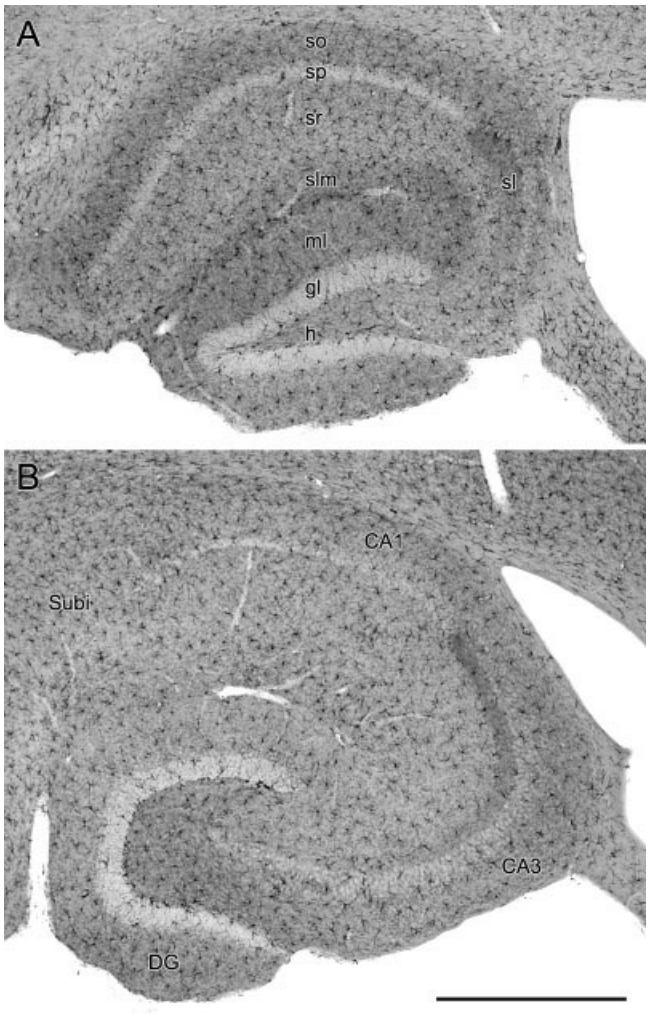

Fig. 3. Iba1 immunostaining in the mouse hippocampus at the dorsal (**A**) and ventral (**B**) levels. Iba1$^+$ microglia are scattered over the whole area of the hippocampus. No apparent dorsoventral differences are observed. Scale bar: B = 500 μm (applies to A and B). gl, granule cell layer; h, hilus; ml, molecular layer; sl, stratum lucidum; slm, stratum lacunosum-moleculare; so, stratum oriens; sp, stratum pyramidale; sr, stratum radiatum; Subi, subiculum.

state have been well described until now (Zimmer et al., 1997): resting microglia exhibit compact cell bodies with branched processes, whereas activated ones show large cell bodies with short thick processes. From the morphological characteristics of Iba1$^+$ microglia seen here, virtually all cells were considered to be at the resting state. However, in some brains, we encountered a few Iba1$^+$ microglia with different shape, i.e., larger somata with intensely labeled processes. These cells were occasionally seen in the hippocampus (1–2 cells per section) and cortical areas. We totally excluded the brains containing such microglia from the present study, because we could not be sure they were at the resting state.

In the mouse hippocampus, Iba1$^+$ microglia were scattered over the all regions both at the dorsal and ventral levels (Figs. 3A,B). Their distribution pattern appeared to be homogeneous, and the dorsoventral difference was not qualitatively noticeable. In the Ammon's horn, Iba1$^+$ microglia were rather evenly distributed throughout layers (Figs. 4A,B). In contrast, in the dentate gyrus, Iba1$^+$ microglia were relatively frequently seen in subgranular zone (the border between granule cell layer and hilus; Fig. 4C). They were also often found in the border between granule cell layer and molecular layer. Few cells were detected from deep inside the granule cell layer.

NDs of Iba1$^+$ Microglia

To quantify the distribution of Iba1$^+$ microglia, we estimated their numerical densities (NDs) in the mouse hippocampus. Here we counted 6,683 Iba1$^+$ microglia from four mice according to the optical disector principle (Table 1). Of these cells, 3,348 were from the dorsal level and 3,335 were from the ventral level.

The statistical significances of dorsoventral differences are summarized in Table 1, and those of interregional and interlaminar differences are summarized in Fig. 5. The NDs of Iba1$^+$ microglia in each region were rather constant ($5.5 \sim 6.0 \times 10^3/mm^3$) in the dorsal hippocampus, but they were somewhat varied in the ventral hippocampus ($4.8 \sim 5.8 \times 10^3/mm^3$). The dorsoventral differences were analyzed by Welch's t-test. No significant dorsoventral differences were observed in the CA1 region and dentate gyrus. But the NDs in the CA3 region were significantly higher at the dorsal level than at the ventral level. The interregional differences were examined using one-way ANOVA with *post hoc* Scheffe's test. There was no significant interregional difference in the dorsal hippocampus ($P = 0.123$; Fig. 5A), whereas a significant difference was detected in the ventral hippocampus ($P = 0.001$; Fig. 5E). *Post hoc* Scheffe's test ($P < 0.05$) performed in the ventral hippocampus revealed that CA1 region and dentate gyrus constituted a homogeneous subset (high density), whereas CA3 region formed a separate subset (low density).

The NDs of Iba1$^+$ microglia in each layer showed no significant dorsoventral differences in the CA1 region and dentate gyrus (Table 1). However, in the CA3 region, the NDs were significantly higher at the dorsal level than at the ventral level in the strata oriens, radiatum, and lacunosum-moleculare. Next, we tested the interlaminar differences in each region. One-way ANOVA revealed that significant interlaminar differences occurred in the CA1 (Figs. 5B,F) and CA3 regions (Figs. 5C,G). In the CA1 region, *post hoc* Scheffe's test ($P < 0.05$) indicated that the four layers constituted two homogeneous subsets in both the dorsal and ventral hippocampi: stratum lacunosum-moleculare formed a single subset (high density) and the remaining three layers, i.e., strata oriens, pyramidale, and radiatum, formed a distinct subset (low density). In the dorsal CA3 region, the five layers constituted three homogeneous subsets: strata lacunosum-moleculare (high density) and lucidum (low density) each constituted a distinct subset, and the remaining layers, i.e., strata oriens, pyramidale, and radiatum, formed a single subset (medium density). In contrast, in the ventral CA3 region, stratum lacunosum-

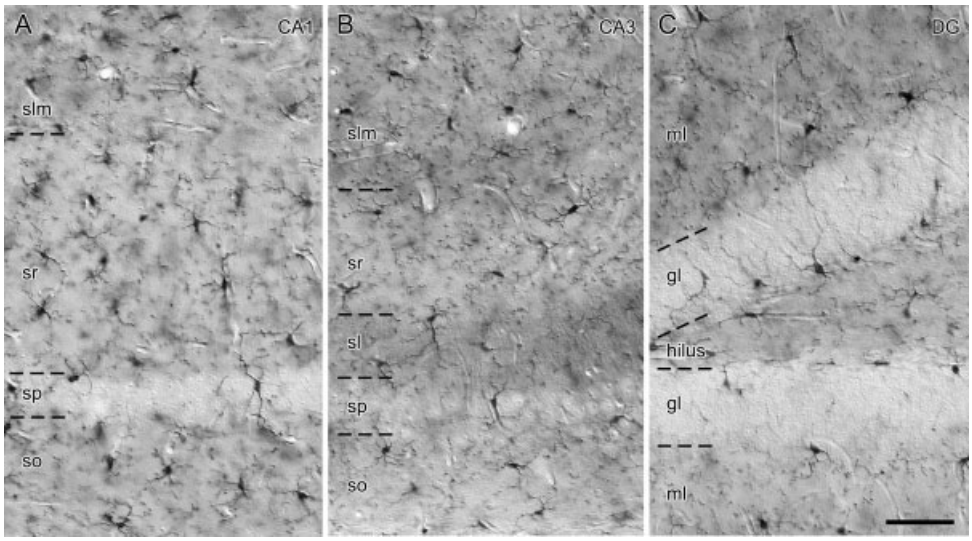

Fig. 4. Nomarski optics photomicrographs showing Iba1 immunostaining in the CA1 (A) and CA3 (B) regions, and the dentate gyrus (C) of the mouse dorsal hippocampus. **A**: Small ramified Iba1$^+$ microglia are uniformly distributed in all layers of the CA1 region. **B**: Similar to the CA1 region, Iba1$^+$ microglia are scattered over the whole area of the CA3 region. **C**: In the dentate gyrus, Iba1$^+$ microglia are rather concentrated in subgranular layer. The occurrence of Iba1$^+$ microglia also increases at the border between granule cell layer and molecular layer. Few Iba1$^+$ microglia enter deep inside the granule cell layer. There are no apparent morphological differences in the CA1 (A) and CA3 (B) regions and dentate gyrus (C). Scale bar: C = 50 μm (applies to A–C). gl, granule cell layer; h, hilus; ml, molecular layer; sl, stratum lucidum; slm, stratum lacunosum-moleculare; so, stratum oriens; sp, stratum pyramidale; sr, stratum radiatum.

TABLE 1. Numerical Densities of Iba1$^+$ Microglia in the Mouse Hippocampus

	Numbers		Numerical densities ($\times 10^3$/mm^3)	
Region	Dorsal	Ventral	Dorsal	Ventral
CA1	1308[a]	1181	6.12 ± 0.53[b]	5.94 ± 0.34
CA3	940	1068	5.99 ± 0.29	4.76 ± 0.27*
DG	1100	1086	5.56 ± 0.13	5.60 ± 0.28
Total	3348	3335	5.89 ± 0.28	5.46 ± 0.30
Layer				
CA1				
So	219	164	5.31 ± 0.10	5.46 ± 0.66
sp	167	235	5.90 ± 0.36	5.76 ± 0.43
sr	516	374	5.96 ± 0.71	5.42 ± 0.35
slm	406	408	7.05 ± 0.92	6.97 ± 0.72
CA3				
so	208	169	5.70 ± 0.19	4.43 ± 0.37*
sp	236	174	5.93 ± 0.33	5.21 ± 0.49
sl	76	93	4.26 ± 0.42	4.39 ± 0.63
sr	195	334	6.07 ± 0.47	4.43 ± 0.43*
slm	225	299	7.28 ± 0.74	5.75 ± 0.28**
DG				
hilus	133	425	5.48 ± 0.30	5.79 ± 0.32
gl	399	300	5.51 ± 0.15	5.86 ± 0.50
ml	568	361	5.61 ± 0.16	5.30 ± 0.55

[a] Values represent the numbers of disector-counted Iba1$^+$ microglia in selected sections.
[b] Values represent the means ± SD among animals (n = 4). The dorsoventral difference is statistically determined by Welch's t-test (*$P < 0.01$ or **$P < 0.05$).

moleculare formed a single subset (high density), and the other layers formed a distinct homogeneous subset (low density). All these results made it clear that Iba1$^+$ microglia are specifically concentrated in the stratum lacunosum-moleculare of the Ammon's horn throughout the longitudinal hippocampal axis. Finally, no significant interlaminar differences were observed in the dentate gyrus of dorsal (P = 0.673; Fig. 5D) and ventral hippocampi (P = 0.231; Fig. 5H).

3D Point Pattern Analysis

To further evaluate the spatial arrangement of Iba1$^+$ microglia in the mouse hippocampus, we carried out a 3D point pattern analysis. In this study, we focused on the CA1 region of the dorsal hippocampus, because its simple laminar organization is advantageous for the point pattern analysis. The distributions of Iba1$^+$ microglia and S100β$^+$ astrocytes contained in a 50-μm-thick section are schematically represented in Fig. 6 as projected 2D distributions. Despite the earlier quantitative results, the distribution of Iba1$^+$ microglia appeared rather homogeneous (Fig. 6A). By contrast, S100β$^+$ astrocytes were more concentrated in the stratum lacunosum-moleculare than in the other layers (Fig. 6B). Close apposition between Iba1$^+$ microglia and S100β$^+$ astrocytes were occasionally found throughout layers (Fig. 6C).

Figure 7 summarizes the results of 3D point pattern analysis for Iba1$^+$ microglia, S100β$^+$ astrocytes and their interrelationship in the whole area of CA1 region. Here we estimated the L-function (Figs. 7A–C), the pair correlation function (Figs. 7D,E) and the nearest neighbor distance distribution function (Fig. 7F). The 90% confidence intervals for a specific distance value were also calculated. Estimates of the averaged value of L-function $L(r)$-r of Iba1$^+$ microglia showed negative value between 0 and 50 μm, which were appreciably different from the confidence intervals (Fig. 7A). The estimated averaged pair correlation function $g(r)$ of Iba1$^+$ microglia was also lower than 1 between 0 and 40 μm (Fig. 7D). Monte Carlo rank test for Poisson process of Iba1$^+$ microglia showed that statistically significant differences from CSR occurred in $L(r)$-r and $g(r)$ estimates (Table 2). These findings indicate that Iba1$^+$ microglia are distrib-

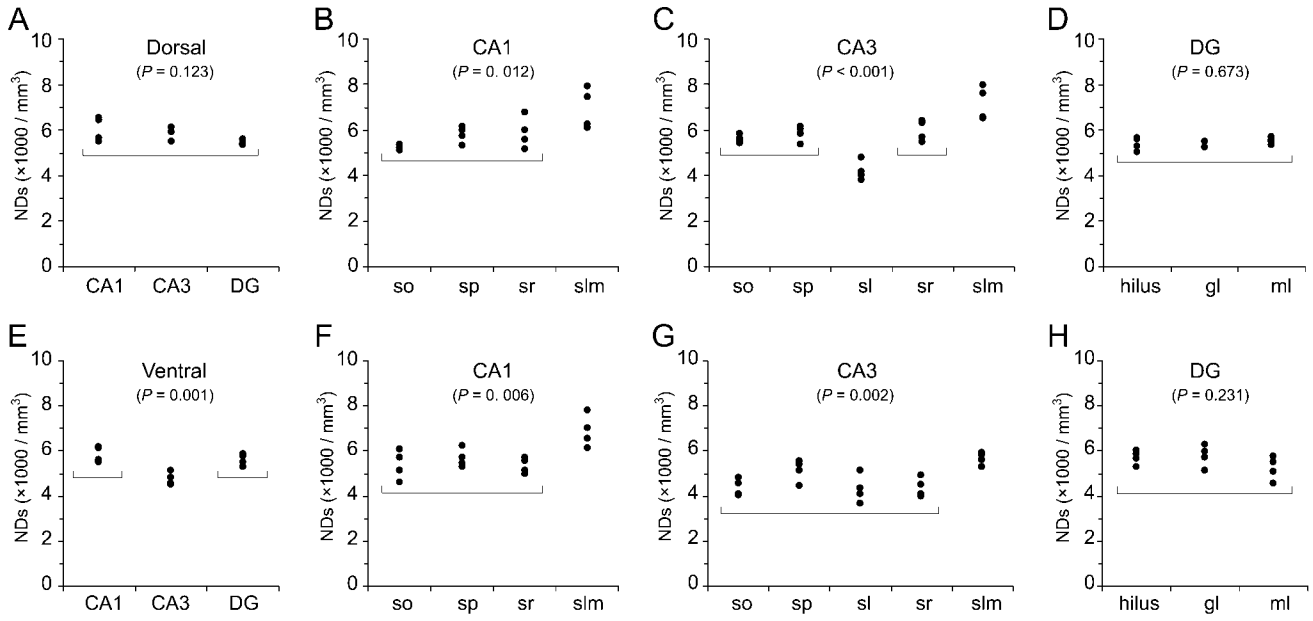

Fig. 5. Graphic representations of the NDs of Iba1$^+$ microglia in the mouse hippocampus at the dorsal (**A–D**) and ventral (**E–H**) levels. Each interregional and interlaminar difference is tested by one-way ANOVA, and the P values are shown in parenthesis. Underbrackets indicate the homogeneous subsets revealed by *post hoc* Scheffe's test ($P < 0.05$).

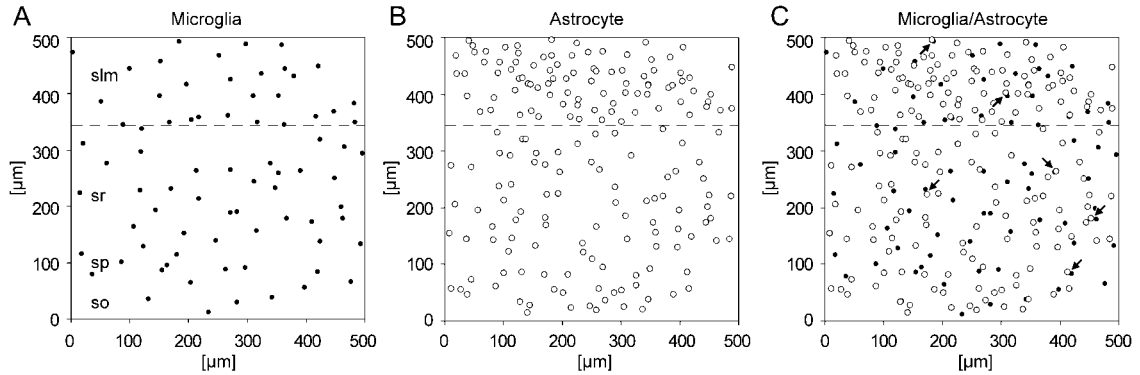

Fig. 6. Schematic representations showing the distribution of Iba1$^+$ microglia (**A**), S100β$^+$ astrocytes (**B**), and both of them (**C**) in the dorsal CA1 region obtained from the projection of a CLSM image stack. The border between stratum lacunosum-moleculare (slm) and stratum radiatum (sr) is indicated by straight line. Arrows indicate the actual contacts between Iba1$^+$ microglia and S100β$^+$ astrocytes confirmed by checking the serial optical sections. The remaining close appositions were artificial, resulting from the procedure of projection. sp, stratum pyramidale; so, stratum oriens.

uted repulsively. Next, the averaged value of $L(r)$-r of S100β$^+$ astrocytes showed a mostly positive slope apart from the hardcore effect because of the limited spatial distribution of imaging and the analysis methods (Fig. 7B). Although there is a region of repulsion for small distance radii, it was not obvious. The frequency of $g(r)$ of S100β$^+$ astrocytes were below 1 between 0 and 18 μm (Fig. 7E). Monte Carlo rank test showed that the statistically significant differences occurred in $L(r)$-r but not in $g(r)$ (Table 2). These results indicate a somewhat repulsive distribution of S100β$^+$ astrocytes. Finally, the averaged value of $L(r)$-r calculated from the interaction between microglia and astrocytes were rather similar to independent behavior (Fig. 7C). The estimated averaged nearest neighbor distance distribution function $D(r)$ from both were almost within the theoretical value for independent behavior (Fig. 7F). Neither $L(r)$-r nor $D(r)$ showed any significant difference in the Monte Carlo rank test (Table 2). Thus, Iba1$^+$ microglia and S100β$^+$ astrocytes were considered to be distributed independently in the whole area of CA1 region.

In spite of the earlier findings, there is a potential that the present results might be adversely affected by uneven laminar distributions of microglia and astrocytes. Especially, the NDs of S100β$^+$ astrocytes in the CA1 region were extensively higher in the stratum lacunosum-moleculare than in the other layers (Ogata and Kosaka, 2002). We therefore arbitrarily divided the dorsal CA1 region into two compartments, i.e., stratum lacunosum-moleculare (slm) and remaining layers (strata ori-

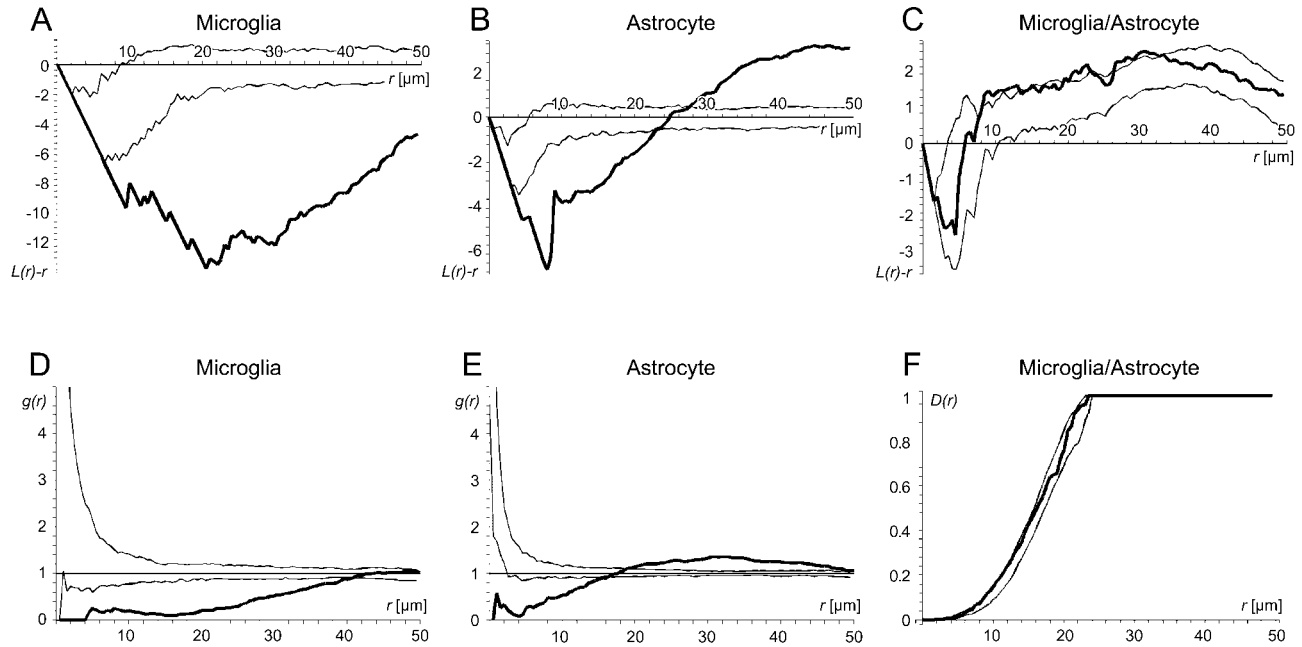

Fig. 7. Averaged estimated values (thick lines) and 90% *r*-wise confidence intervals (thin lines) for *L*-function (**A–C**), pair correlation function (**D,E**), and nearest neighbor distance distribution function (**F**). Each graph is derived from Iba1$^+$ microglia (A,D), S100β$^+$ astrocytes (B,E), and their interaction (C,F) in the CA1 region of the dorsal hippocampus.

TABLE 2. Summary of Point Pattern Analysis for Iba1$^+$ Microglia and S100β$^+$ Astrocytes

Variables	Whole	slm	so-r
Numbers of microglia	83.9 ± 6.0[a]	30.8 ± 5.1	53.1 ± 5.9
Numbers of astrocytes	219.5 ± 28.8[b]	106.9 ± 20.4	112.6 ± 12.8
Monte Carlo rank test			
L-Function for microglia	100[c]	100	100
L-Function for astrocytes	100	100	100
L-Function for both	71	59	99
Pair correlation function for microglia	100	95	96
Pair correlation function for astrocytes	92	79	85
Pair correlation function for both	–	36	93
Nearest neighbor distance for both	57	–	–

The cells were sampled from the dorsal CA1 region in accordance with the optical disector.
[a] Values represent the numbers of disector-counted Iba1$^+$ microglia, which are expressed as means ± SD (n = 9 sections).
[b] Values represent the numbers of disector-counted S100β$^+$ astrocytes, which are expressed as means ± SD (n = 9 sections).
[c] The data show the results of Monte Carlo rank test for Poisson process. P value = (100 − rank)/100.
slm, stratum lacunosum-moleculare; so-r, stratum oriens, pyramidale and radiatum; –, not tested due to technical limitations.

ens, pyramidale, and radiatum, so-r), and estimated the *L*-function and the pair correlation function separately. The estimated values of $L(r)$-r and $g(r)$ of Iba1$^+$ microglia showed considerably repulsing behavior both in the slm and so-r (Figs. 8A,D). The region of repulsiveness defined by $g(r)$ was 32–38 μm in the slm and 38–42 μm in the so-r. Monte Carlo rank test for Poisson process confirmed the statistically significant differences both in the slm and so-r (Table 2). Next, estimates of $L(r)$-r and $g(r)$ revealed the slightly repulsive distribution of S100β$^+$ astrocytes (Figs. 8B,E). The frequency of $g(r)$ showed the region of repulsiveness about 10–14 μm in the slm and 20–24 μm in the so-r. The statistically significant differences were detected in $L(r)$-r, although no significances were seen in $g(r)$ (Table 2). Finally, the estimated value of $L(r)$-r for interactions between Iba1$^+$ microglia and S100β$^+$ astrocytes exhibited significant deviation from independent behavior in the so-r, but not in the slm (Fig. 8C; Table 2). The frequency of $g(r)$ showed a slight deviation (not statistically significant) from independent behavior in the so-r, but not in the slm (Fig. 8F; Table 2). These findings indicate that Iba1$^+$ microglia and S100β$^+$ astrocytes are attracted in the so-r, whereas they seem to be independent in the slm.

DISCUSSION

This study provides a rigorous quantitative description on the spatial arrangement of resting microglia in the mouse hippocampus. The main findings can be summarized as follows: (1) The NDs of Iba1$^+$ microglia in the ventral hippocampus were significantly lower in the

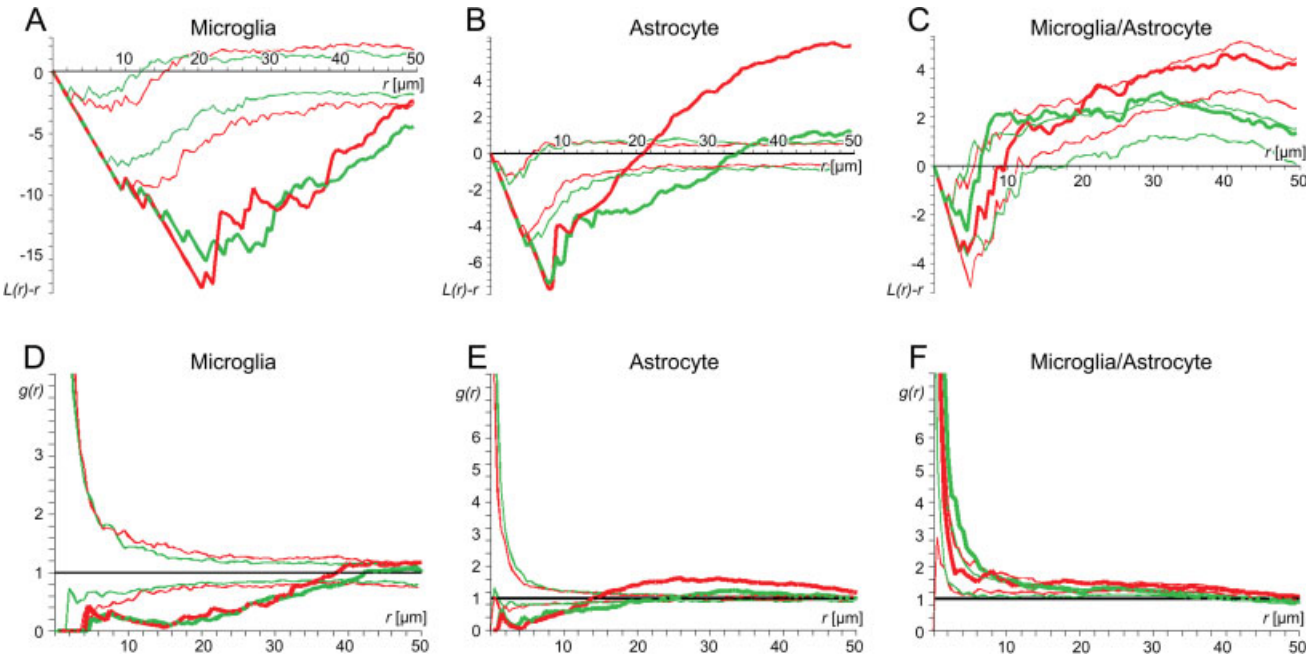

Fig. 8. Averaged estimated values (thick lines) and 90% *r*-wise confidence intervals (thin lines) for *L*-function (**A–C**) and pair correlation function (**D–F**). Each graph is derived from Iba1$^+$ microglia (A,D), S100β$^+$ astrocytes (B,E), and their interaction (C,F) in the CA1 region of the dorsal hippocampus. Red lines show the data of stratum lacunosum-moleculare, green lines show the total data of the remaining layers, i.e., strata oriens, pyramidale and radiatum.

CA3 region than in the CA1 region and dentate gyrus, although no interregional differences were detectable in the dorsal hippocampus. (2) In the Ammon's horn, the NDs were significantly higher in the stratum lacunosum-moleculare than in the other layers both at the dorsal and ventral levels. (3) In the CA3 region, the NDs in the strata oriens, radiatum and lacunosum-moleculare were significantly higher at the dorsal level than at the ventral level. (4) The 3D point pattern analysis demonstrated that each of Iba1$^+$ microglia and S100β$^+$ astrocyte was repulsively distributed in the CA1 region. (5) The localization of Iba1$^+$ microglia and S100β$^+$ astrocytes was supposed to be independent with respect to each other in the stratum lacunosum-moleculare, but attracted in the remaining layers of the CA1 region.

Methodological Considerations

Various important questions in neuroscience cannot be answered only by qualitative analysis (for review see, Schmitz and Hof, 2005). The major advantage of our quantitative study is the application of stereology for the estimation of NDs and 3D coordinates of microglia. As reported previously, the chief problem of conventional 2D approach is that the detection efficiency of objects is related to their size, shape, and orientations. For instance, larger objects are potentially counted more frequently than smaller objects, and such sampling biases are usually uncorrectable. However, the use of stereology with 3D probes enables a rigorous quantification without biases (Sterio, 1984). The optical disector is one of the modern assumption-free stereological techniques, which is particularly suitable for strict analysis using thick immunostained sections (Braendgaard et al., 1990). Therefore, it is no exaggeration to say that the present quantitative data gives an essential anatomical basis of neuroscience.

Here we selected Iba1 as a marker of microglia in the mouse hippocampus. Many other molecular markers have been used to identify microglia in earlier studies. However, Iba1 has some advantages over other markers. For instance, Wu et al. (1992) used lectin to detect microglia in the rat corpus callosum, but heavy lectin labeling of blood vessels resulted in difficulties with identification of microglial cell bodies. Savchenko et al. (2000) showed that lipocortin 1 was a specific microglial marker in the adult rat brain. Nevertheless, lipocortin 1 was not detected in healthy mouse brain (Williams et al., 1997). Mac-1 is an established microglial marker. However, because of its rim-like staining of soma, Mac-1 was not useful for counting microglial cell bodies (see earlier). Taken together with these findings and its superb visibility throughout the thick preparations, we consider that Iba1 is an excellent microglial marker.

It has been reported that the expression of Iba1 is upregulated in activated microglia by noxious stimuli, such as ischemia (Ito et al., 2001) and epilepsy (Drage et al., 2002). In other words, Iba1 may be down-regulated in microglia at the resting state. This concern leads us to question whether Iba1 can label all of the resting microglia. Our double immunofluorescence experiment for Iba1 and Mac-1 gives some answer to this inquiry. Mac-1 is also called CD11b, which belongs to β-2 integrin family (Kishimoto et al, 1987). Previous studies showed that

Mac-1 was consistently expressed in brain microglia at the resting as well as the activated state (Akiyama and McGeer, 1990). Although there were some differences in their subcellular localization, Iba1 and Mac-1 were almost always coexpressed in microglial cell bodies. We therefore are able to claim that the present study exactly quantified the microglia at the resting state.

NDs of Iba1$^+$ Microglia in the Mouse Hippocampus

There are several papers providing a quantitative description of microglia in the hippocampus. However, most of them employed a nonstereological method, and usually reported the data as numbers of cells per unit area (Lawson et al., 1990; Savchenko et al., 2000). Considering the 3D organization of brain, such 2D data is of limited significance. Instead, here we stereologically estimated the NDs (i.e., numbers of cells per unit volume) of microglia. Two previous studies reported the stereological quantification of Mac-1$^+$ microglia in the mouse hippocampus using the fractionator (Long et al., 1998; Wirenfeldt et al., 2003). Although the main interest of these reports was the total number of microglia in the hippocampus, the former study also estimated the NDs of microglia in the CA1 region ($22.3 \times 10^3/mm^3$) and in the dentate gyrus ($18.8 \times 10^3/mm^3$). These values are more than twice as high as our data, but the reason of discrepancy between two studies is simple: tissue shrinkage was not corrected in the paper of Long et al. (1998). But fortunately, the section thickness before and after the histological processing was described in that paper, and thus we could calculate the NDs by using the thickness shrinkage factor. The corrected NDs of Mac-1$^+$ microglia were estimated to be $7.7 \times 10^3/mm^3$ in the CA1 region and $7.0 \times 10^3/mm^3$ in the dentate gyrus. As a comparison, the NDs of GFP-labeled microglia in the mouse neocortex were $6.5 \times 10^3/mm^3$ in layer 1 and $6.4 \times 10^3/mm^3$ in layer 2/3 (Nimmerjahn et al., 2005). These data are rather similar to our results, and may support the validity of present data obtained from Iba1 immunocytochemistry.

Considering the role of microglia as housekeeper, the homogenous distribution seems to be most suitable for them. However, the present quantitative analysis revealed the statistically significant dorsoventral, interregional and interlaminar differences in the NDs of Iba1$^+$ microglia. For instance, Welch's *t*-test showed that the NDs in the CA3 region were significantly higher at the dorsal level than at the ventral level. One-way ANOVA showed that the NDs were significantly lower in the CA3 region than in the CA1 region and dentate gyrus in the ventral hippocampus. The *post hoc* Scheffe's test demonstrated that the NDs were significantly higher in the stratum lacunosum-moleculare than in the remaining layers for each region of the Ammon's horn. At least two possible explanations can be offered to the heterogenous distribution of microglia. First, these variations in the NDs of Iba1$^+$ microglia might be related to the vulnerability of the hippocampus. The ventral hippocampus is known to be more seizure prone than the dorsal hippocampus (Racine et al., 1977), and the NDs of Iba1$^+$ microglia were lower in the ventral level than in the dorsal level. The epileptic activity causes severe spine loss of CA3 pyramidal neurons (Drakew et al., 1996), and the NDs of Iba1$^+$ microglia were lower in the CA3 region than in the CA1 region and dentate gyrus. These findings suggest that microglial density might be involved in the site-specific vulnerability of the hippocampus. Second, the heterogeneous distribution of microglia would participate in the modulation of hippocampal neuronal activity. Dalmau et al. (1998) reported that the occurrence of microglia in each hippocampal layer corresponded well to the maturation of synaptic structure. Wang et al. (2004) demonstrated that nitric oxide produced by microglia was involved in long-term potentiation in the hippocampus. Because of the limited scope of the present article, the microglial density described here gives only speculative significance, but will be more meaningful in combination with more comprehensive studies (such as experiments using genetic models for human diseases) in the near future.

Spatial Arrangement of Microglia and Astrocytes

Earlier point pattern analyses evaluated the distribution of neurons and glial cells based on the 2D coordinates (Diggle, 1986; Distler et al., 1991). However, the importance of 3D point pattern analysis has been emphasized in recent studies (Beil et al., 2005; Schmitz et al., 2002). We therefore determined the 3D coordinates of Iba1$^+$ microglia and S100β^+ astrocytes from stacks of CLSM optical sections in accordance with the optical disector principle. Furthermore, to prevent the bias caused by the shrinkage of preparations because of the histological procedure, we corrected the 3D coordinates by the shrinkage factors (Jinno et al., 1998) in advance. These procedures will become basic requirements for the point pattern analysis.

Both *L*-function and pair correlation function indicate that microglia are distributed repulsively. Because microglia have been shown to be continuously assessing local microenvironment even at the resting state, the repulsive arrangement of resting microglia is well suited for accomplishing such a housekeeping task efficiently and specifically. Considering that the cell bodies of resting microglia are stable in the adult brain, the distribution of microglia in the hippocampus seems to be repulsively arranged during the developmental stage. To better understand the spatial arrangement of microglia, we summarize three theoretical territories occupied by a single microglia in Fig. 9A. The first territory was estimated from the NDs of Iba1$^+$ microglia by assuming constant microglial size. In the stratum radiatum of the dorsal CA1 region, for example, the assigned volume of a single microglia was 166.1×10^{-6} mm^3, and thus the ECR was 34.1 μm. The second territory was obtained from the process tracing of Iba1$^+$ microglia (ECR = 32.3 μm). Although we could not deny the possibility of partial immunostaining of microglia, we considered that the fine processes with bulbous endings identified by Iba1 gave

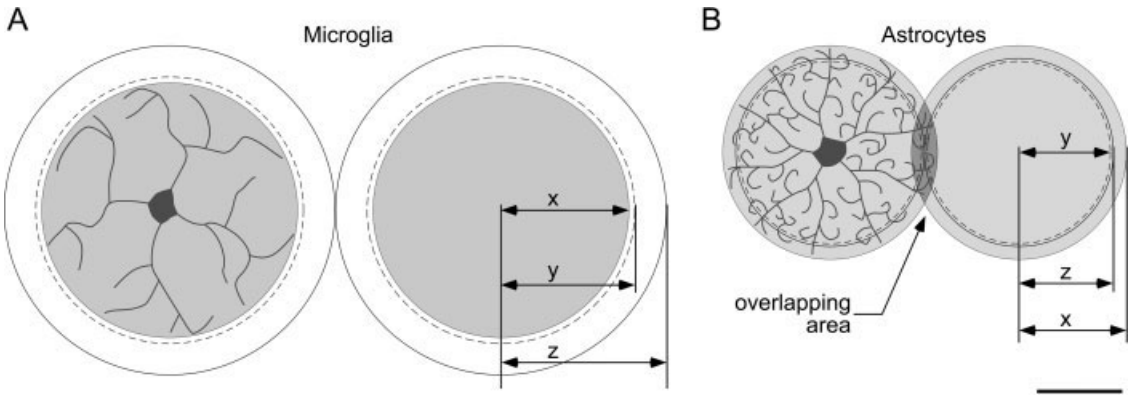

Fig. 9. Schematic drawings of the spatial arrangement of microglia (A) and astrocytes (B). The data is obtained from the stratum radiatum of the CA1 area. **A**: Pairs of concentric circles represent three theoretical territories of a single microglia, i.e., the area occupied by Iba1$^+$ processes (x = 32.2 μm), the assigned region calculated from the NDs (y = 34.1 μm) and the region of repulsiveness defined by pair correlation function $g(r)$ (z = 42 μm). The cells are tentatively contacted with the territories defined by $g(r)$, and there is a free space between neighboring microglia. **B**: Pairs of three concentric circles represent three theoretical territories of a single astrocyte, i.e., the area occupied by intracellular labeling (x = 27.3 μm, Ogata and Kosaka, 2002), the assigned region calculated from the NDs (y = 23.7 μm, Ogata and Kosaka, 2002) and the region of repulsiveness defined by $g(r)$ (z = 24 μm). The cells are contacted with the territories defined by $g(r)$ same as earlier, and an overlapping area (shaded) appears. Scale bar: B = 20 μm (applies to A and B).

proof of their practically perfect visualization. The third territory was extrapolated from the point pattern analysis: the region of repulsiveness defined by $g(r)$ was considerably large, about 42 μm (Fig. 8D). These findings indicate that microglia are not touching each other with their processes, because the cells are packed in a sphere defined by $g(r)$. Considering that microglial processes survey the extracellular space in a seemingly random fashion, and not always screen whole area of its territory (see Fig. 1A of Nimmerjahn et al., 2005), such process-free space at a certain instant might be reasonable.

As for the spatial arrangement of astrocytes, earlier point pattern analyses have reported their repulsive distribution based on the estimation of nearest neighbor distance distribution function (Distler et al., 1991, 1993). These studies postulated the idea of contact spacing (Chan-Ling and Stone, 1991): close contact of the astrocyte processes resulted in the repulsion between the somata of neighbors. With this clue to go on, recent studies demonstrated the domain formation of astrocytes (Bushong et al., 2002; Ogata and Kosaka, 2002; Wilhelmsson et al., 2006). In the present study, we also found the slightly repulsive distribution of S100β$^+$ astrocytes employing the L-function and the pair correlation function. In addition, we suggest three theoretical territories occupied by a single astrocyte in combination with our previous report (Ogata and Kosaka, 2002) and the present data (Fig. 9B). In the stratum radiatum of the dorsal CA1 region, for instance, the ECR of astrocytes calculated from the NDs was 23.7 μm, whereas that defined by the intracellular labeling was 27.3 μm [Ogata and Kosaka (2002) mistakenly used "diameter" instead of "radius" in the legend of Table 2]. Because ECR assigned by the ND was smaller than that estimated from the process tracing, substantial interdigitation between neighboring astrocytes was advocated by Ogata and Kosaka (2002). What has to be noticed here is that the region of repulsiveness defined by $g(r)$ was about 24 μm (Fig. 8E), which was also smaller than ECR defined by intracellular labeling. These findings might indicate the existence of overlapping areas of astrocyte territories and support the idea concerning interdigitation between repulsively allocated neighboring astrocytes. Interestingly, a recent study (Bushong et al., 2004) has reported that developing astrocytes are not repulsed by contact with homotypic processes. Bushong et al. (2004) indicated that domain formation was largely the consequence of competition between astrocyte processes. We therefore suggest that there might be distinct mechanisms regulating the formation of astrocyte territories and the repulsive localization of cell bodies.

Earlier studies have reported the interaction of microglia and astrocytes through various factors, but the detailed mechanisms have not yet been established. In this study, we encountered the close apposition between these two types of glial cells via somata and processes. Furthermore, the Monte Carlo rank test using the L-function for Poisson processes indicate that a significant attraction between microglia and astrocytes occurred in the strata oriens, pyramidale and radiatum of the CA1 region. Although further analysis will be required, the present findings provide a key to understand the interrelationship between astrocytes and microglia.

ACKNOWLEDGMENTS

The authors are grateful to Dr. Eric Bushong for his critical reading and grammatical corrections. We also thank Miss C. Goto for her secretarial assistance.

REFERENCES

Akiyama H, McGeer PL. 1990. Brain microglia constitutively express β-2 integrins. J Neuroimmunol 30:81–93.
Aloisi F. 2001. Immune function of microglia. Glia 36:165–179.

Baddeley AJ. 1998. Spatial sampling and sensoring. In: Kendall WS, Lieshout MNM, van Barndorf-Nielsen OE, editors. Current trends in stochastic geometry and its applications. London: Chapman and Hall. pp 37–78.

Beil M, Fleischer F, Paschke S, Schmidt V. 2005. Statistical analysis of the three-dimensional structure of centromeric heterochromatin in interphase nuclei. J Microsc 217 (Part 1):60–68.

Braendgaard H, Evans SM, Howard CV, Gundersen HJ. 1990. The total number of neurons in the human neocortex unbiasedly estimated using optical disectors. J Microsc 157 (Part 3):285–304.

Bushong EA, Martone ME, Ellisman MH. 2004. Maturation of astrocyte morphology and the establishment of astrocyte domains during postnatal hippocampal development. Int J Dev Neurosci 22:73–86.

Bushong EA, Martone ME, Jones YZ, Ellisman MH. 2002. Protoplasmic astrocytes in CA1 stratum radiatum occupy separate anatomical domains. J Neurosci 22:183–192.

Chan-Ling T, Stone J. 1991. Factors determining the migration of astrocytes into the developing retina: Migration does not depend on intact axons or patent vessels. J Comp Neurol 303:375–386.

Dalmau I, Finsen B, Zimmer J, Gonzalez B, Castellano B. 1998. Development of microglia in the postnatal rat hippocampus. Hippocampus 8:458–474.

Davalos D, Grutzendler J, Yang G, Kim JV, Zuo Y, Jung S, Littman DR, Dustin ML, Gan WB. 2005. ATP mediates rapid microglial response to local brain injury *in vivo*. Nat Neurosci 8:752–758.

Diggle PJ. 1986. Displaced amacrine cells in the retina of a rabbit: Analysis of a bivariate spatial point pattern. J Neurosci Methods 18:115–125.

Diggle PJ. 2003. Statistical analysis of spatial point patterns. London: Arnold.

Distler C, Dreher Z, Stone J. 1991. Contact spacing among astrocytes in the central nervous system: An hypothesis of their structural role. Glia 4:484–494.

Distler C, Weigel H, Hoffmann KP. 1993. Glia cells of the monkey retina. I. Astrocytes. J Comp Neurol 333:134–147.

Drage MG, Holmes GL, Seyfried TN. 2002. Hippocampal neurons and glia in epileptic EL mice. J Neurocytol 31:681–692.

Drakew A, Muller M, Gahwiler BH, Thompson SM, Frotscher M. 1996. Spine loss in experimental epilepsy: Quantitative light and electron microscopic analysis of intracellularly stained CA3 pyramidal cells in hippocampal slice cultures. Neuroscience 70:31–45.

Effron B, Tibshirani RJ. 1994. An introduction to the bootstrap. New York: Chapman and Hall.

Hailer NP, Jarhult JD, Nitsch R. 1996. Resting microglial cells *in vitro*: Analysis of morphology and adhesion molecule expression in organotypic hippocampal slice cultures. Glia 18:319–331.

Hanisch KH. 1984. Some remarks on estimators of the distribution function of nearest-neighbor distance in stationary spatial point patterns. Statistics 15:409–412.

Haynes SE, Hollopeter G, Yang G, Kurpius D, Dailey ME, Gan WB, Julius D. 2006. The P2Y(12) receptor regulates microglial activation by extracellular nucleotides. Nat Neurosci 9:1512–1519.

Horner PJ, Palmer TD. 2003. New roles for astrocytes: The nightlife of an 'astrocyte'. La vida loca! Trends Neurosci 26:597–603.

Hsu SM, Raine L, Fanger H. 1981. Use of avidin–biotin–peroxidase complex (ABC) in immunoperoxidase techniques: A comparison between ABC and unlabeled antibody (PAP) procedures. J Histochem Cytochem 29:577–580.

Imai Y, Ibata I, Ito D, Ohsawa K, Kohsaka S. 1996. A novel gene iba1 in the major histocompatibility complex class III region encoding an EF hand protein expressed in a monocytic lineage. Biochem Biophys Res Commun 224:855–862.

Ito D, Tanaka K, Suzuki S, Dembo T, Fukuuchi Y. 2001. Enhanced expression of Iba1, ionized calcium-binding adapter molecule 1, after transient focal cerebral ischemia in rat brain. Stroke 32:1208–1215.

Jinno S, Aika Y, Fukuda T, Kosaka T. 1998. Quantitative analysis of GABAergic neurons in the mouse hippocampus, with optical disector using confocal laser scanning microscope. Brain Res 814:55–70.

Jinno S, Kosaka T. 2002. Patterns of expression of calcium binding proteins and neuronal nitric oxide synthase in different populations of hippocampal GABAergic neurons in mice. J Comp Neurol 449:1–25.

Kishimoto TK, Hollander N, Roberts TM, Anderson DC, Springer TA. 1987. Heterogeneous mutations in the β subunit common to the LFA-1, Mac-1, and p150,95 glycoproteins cause leukocyte adhesion deficiency. Cell 50:193–202.

Lawson LJ, Perry VH, Dri P, Gordon S. 1990. Heterogeneity in the distribution and morphology of microglia in the normal adult mouse brain. Neuroscience 39:151–170.

Long JM, Kalehua AN, Muth NJ, Hengemihle JM, Jucker M, Calhoun ME, Ingram DK, Mouton PR. 1998. Stereological estimation of total microglia number in mouse hippocampus. J Neurosci Methods 84:101–108.

Ludwin SK, Kosek JC, Eng LF. 1976. The topographical distribution of S100 and GFA proteins in the adult rat brain: An immunohistochemical study using horseradish peroxidase-labelled antibodies. J Comp Neurol 165:197–207.

Mattfeldt T, Fleischer F. 2005. Bootstrap methods for statistical inference from stereological estimates of volume fraction. J Microsc 218:160–170.

Mayer J, Schmidt V, Schweiggert F. 2004. A unified simulation framework for spatial stochastic models. Simulat Model Pract Theor 12:307–326.

Mohri I, Taniike M, Taniguchi H, Kanekiyo T, Aritake K, Inui T, Fukumoto N, Eguchi N, Kushi A, Sasai H, Kanaoka Y, Ozono K, Narumiya S, Suzuki K, Urade Y. 2006. Prostaglandin D2-mediated microglia/astrocyte interaction enhances astrogliosis and demyelination in twitcher. J Neurosci 26:4383–4393.

Nimmerjahn A, Kirchhoff F, Helmchen F. 2005. Resting microglial cells are highly dynamic surveillants of brain parenchyma *in vivo*. Science 308:1314–1318.

Ogata K, Kosaka T. 2002. Structural and quantitative analysis of astrocytes in the mouse hippocampus. Neuroscience 113:221–233.

Perry VH, Hume DA, Gordon S. 1985. Immunohistochemical localization of macrophages and microglia in the adult and developing mouse brain. Neuroscience 15:313–326.

Racine R, Rose PA, Burnham WM. 1977. After discharge thresholds and kindling rates in dorsal and ventral hippocampus and dentate gyrus. Can J Neurol Sci 4:273–278.

Rickmann M, Wolff JR. 1995. S100 protein expression in subpopulations of neurons of rat brain. Neuroscience 67:977–991.

Savchenko VL, McKanna JA, Nikonenko IR, Skibo GG. 2000. Microglia and astrocytes in the adult rat brain: Comparative immunocytochemical analysis demonstrates the efficacy of lipocortin 1 immunoreactivity. Neuroscience 96:195–203.

Schmitz C, Grolms N, Hof PR, Boehringer R, Glaser J, Korr H. 2002. Altered spatial arrangement of layer V pyramidal cells in the mouse brain following prenatal low-dose X-irradiation. A stereological study using a novel three-dimensional analysis method to estimate the nearest neighbor distance distributions of cells in thick sections. Cereb Cortex 12:954–960.

Schmitz C, Hof PR. 2005. Design-based stereology in neuroscience. Neuroscience 130:813–831.

Schwartz M, Butovsky O, Bruck W, Hanisch UK. 2006. Microglial phenotype: Is the commitment reversible? Trends Neurosci 29:68–74.

Solà C, Casal C, Tusell JM, Serratosa J. 2002. Astrocytes enhance lipopolysaccharide-induced nitric oxide production by microglial cells. Eur J Neurosci 16:1275–1283.

Sterio DC. 1984. The unbiased estimation of number and sizes of arbitrary particles using the disector. J Microsc 134 (Part 2):127–136.

Stoyan D, Stoyan H. 1994. Fractals, random shapes and point fields. Chichester: Wiley.

Stoyan D, Stoyan H, Tscheschel A, Mattfeldt T. 2001. On the estimation of distance distribution functions for point processes and random sets. Image Anal Stereol 20:65–69.

Vela JM, Dalmau I, Gonzalez B, Castellano B. 1995. Morphology and distribution of microglial cells in the young and adult mouse cerebellum. J Comp Neurol 361:602–616.

Verderio C, Matteoli M. 2001. ATP mediates calcium signaling between astrocytes and microglial cells: Modulation by IFN-γ. J Immunol 166:6383–6391.

von Bernhardi R, Ramirez G. 2001. Microglia–astrocyte interaction in Alzheimer's disease: Friends or foes for the nervous system? Biol Res 34:123–128.

Wang Q, Rowan MJ, Anwyl R. 2004. β-Amyloid-mediated inhibition of NMDA receptor-dependent long-term potentiation induction involves activation of microglia and stimulation of inducible nitric oxide synthase and superoxide. J Neurosci 24:6049–6056.

Wilhelmsson U, Bushong EA, Price DL, Smarr BL, Phung V, Terada M, Ellisman MH, Pekny M. 2006. Redefining the concept of reactive astrocytes as cells that remain within their unique domains upon reaction to injury. Proc Natl Acad Sci USA 103:17513–17518.

Williams A, Van Dam AM, Ritchie D, Eikelenboom P, Fraser H. 1997. Immunocytochemical appearance of cytokines, prostaglandin E2 and lipocortin-1 in the CNS during the incubation period of murine scrapie correlates with progressive PrP accumulations. Brain Res 754:171–180.

Wirenfeldt M, Dalmau I, Finsen B. 2003. Estimation of absolute microglial cell numbers in mouse fascia dentata using unbiased and efficient stereological cell counting principles. Glia 44:129–139.

Wu CH, Wen CY, Shieh JY, Ling EA. 1992. A quantitative and morphometric study of the transformation of amoeboid microglia into ramified microglia in the developing corpus callosum in rats. J Anat 181 (Part 3):423–430.

Zimmer LA, Ennis M, Shipley MT. 1997. Soman-induced seizures rapidly activate astrocytes and microglia in discrete brain regions. J Comp Neurol 378:482–492.